INSTITUTE OF PHYSICS PUBLISHING PHYSICS IN MEDICINE AND BIOLOGY

Phys. Med. Biol. **47** (2002) 1143–1160 PII: S0031-9155(02)31209-0

Fuzzy clustering-based segmented attenuation correction in whole-body PET imaging

H Zaidi[1], **M Diaz-Gomez**[1], **A Boudraa**[2] **and D O Slosman**[1]

[1] Division of Nuclear Medicine, Geneva University Hospital, CH-1211 Geneva, Switzerland
[2] Ecole Navale, Département Signal, Lanvéoc Poulmic BP600, F 29240 Brest Naval, France

E-mail: habib.zaidi@hcuge.ch

Received 26 November 2001
Published 20 March 2002
Online at stacks.iop.org/PMB/47/1143

Abstract

Segmented attenuation correction is now a widely accepted technique to reduce noise propagation from transmission scanning in positron emission tomography (PET). In this paper, we present a new method for segmenting transmission images in whole-body scanning. This reduces the noise in the correction maps while still correcting for differing attenuation coefficients of specific tissues. Based on the fuzzy C-means (FCM) algorithm, the method segments the PET transmission images into a given number of clusters to extract specific areas of differing attenuation such as air, the lungs and soft tissue, preceded by a median filtering procedure. The reconstructed transmission image voxels are, therefore, segmented into populations of uniform attenuation based on knowledge of the human anatomy. The clustering procedure starts with an over-specified number of clusters followed by a merging process to group clusters with similar properties (redundant clusters) and removal of some undesired substructures using anatomical knowledge.

The method is unsupervised, adaptive and allows the classification of both pre- or post-injection transmission images obtained using either coincident ^{68}Ge or single-photon ^{137}Cs sources into main tissue components in terms of attenuation coefficients. A high-quality transmission image of the scanner bed is obtained from a high statistics scan and added to the transmission image. The segmented transmission images are then forward projected to generate attenuation correction factors to be used for the reconstruction of the corresponding emission scan. The technique has been tested on a chest phantom simulating the lungs, heart cavity and the spine, the Rando–Alderson phantom, and whole-body clinical PET studies showing a remarkable improvement in image quality, a clear reduction of noise propagation from transmission into emission data allowing for reduction of transmission scan duration. There was very good correlation ($R^2 = 0.96$) between maximum standardized uptake values (SUVs) in lung nodules measured on images reconstructed with measured and segmented attenuation correction with a statistically significant

decrease in SUV ($17.03\% \pm 8.4\%$, $P < 0.01$) on the latter images, whereas no proof of statistically significant differences on the average SUVs was observed. Finally, the potential of the FCM algorithm as a segmentation method and its limitations as well as other prospective applications of the technique are discussed.

1. Introduction

Attenuation correction (AC) in positron emission tomography (PET) represents a key step in the reconstruction process and is now widely accepted by the nuclear medicine community as an essential component of the long chain of modules required for the reconstruction of artefact-free, quantitative data. AC has been shown to improve image quality, lesion detection, staging and management of patients in clinical oncology compared to non-attenuation corrected images (Lonneux *et al* 1999). Traditionally, PET transmission measurements are usually acquired in two-dimensional (2D) mode with positron-emitting (^{68}Ga/^{68}Ge) rotating rod sources. Blank (without the patient in the field-of-view) and transmission (with the patient in the field-of-view) scans are acquired and the ratio calculated, generally after some spatial filtering, to reduce statistical variations in the data sets. The attenuation correction factor (ACF) for a given line of response is calculated as the ratio of the blank count rate and transmission count rate. The higher count rate capability resulting from the decreased detector dead time and increased object penetration substantiates the recent interest in single-photon sources such as ^{137}Cs ($E_\gamma = 662$ keV). Since ^{137}Cs has a higher energy photon than the 511 keV from the emission annihilation radiation, the measured transmission must be scaled to account for the difference. This is relatively straightforward and a simple exponent can be used (Bailey 1998).

Noise from the transmission scan will spread through the reconstruction process, affecting the quality of the images. To minimize this effect, long transmission scans are normally acquired to ensure good statistics at the expense of patient comfort especially in the case of whole-body scanning on low-sensitivity partial-ring PET tomographs. During the last decade, techniques based on transmission image segmentation and tissue classification tools have been proposed to minimize the acquisition time (less than 5 min) and increase the accuracy of AC, while still preserving or even reducing the noise level (Anderson *et al* 1999, Reutte *et al* 1997, Riddell *et al* 1999, Yu and Nahmias 1996). Segmentation algorithms must reach equilibrium between the final image quality and computational time. The majority of segmentation methods used for AC fall into one of the following two classes: histogram-based thresholding techniques (Meikle *et al* 1993, Xu *et al* 1994, 1996) and fuzzy-segmentation techniques (Zaidi *et al* 2001, Bettinardi *et al* 1999). Threshold approaches use the grey-level histogram counts to distinguish between regions (Bilger *et al* 2001); however, if the histogram is the sole input source, the technique is most likely to fail in regions where the total number of counts is small (e.g. the skull). Their performance strongly depends on the choice of the thresholds.

Fuzzy-segmentation techniques on the other hand demonstrated excellent performance and produced good results as an automated, unsupervised tool for segmenting noisy images in a robust manner (Zaidi *et al* 2001, Action *et al* 1999, Bettinardi *et al* 1999, Boudraa *et al* 1996, 2000). They are iterative procedures that minimize an objective function. As an output, a membership degree is assigned to every voxel with respect to a cluster centre. Among the algorithms which belong to this class is the fuzzy C-means (FCM) clustering algorithm developed in the 1970s (Dunn 1974) and extended later (Bezdek 1973, Bezdek *et al* 1987).

The number of clusters is normally passed as an input parameter. To automate the process, a cluster validity index can be used to select the optimal number of clusters (Pal and Bezdek 1995, Xie and Beni 1991).

It is recognized that the FCM is sensitive to noise and outliers. To handle the problem of noise, the possibilistic C-means (PCM) (Krishnapuram and Keller 1993) or maximum entropy principle-based fuzzy clustering (MEPFC) (Beni and Liu 1994) algorithms can be used. PCM assumes that the membership function of a point in a fuzzy set (or cluster) is absolute, i.e. it is an evaluation of a degree of typicality not depending on the membership values of the same point in other clusters. In contrast, clustering approaches including the FCM and MEPFC impose a probabilistic constraint, according to which the sum of the membership values of a point in all the clusters must be equal to 1. The PCM algorithm treats each cluster independently of the rest and can thus provide several identical prototypes while completely failing to detect some other clusters. Furthermore, PCM is heavily dependent on initialization and its 'bandwidth parameter', η, is difficult to estimate. It was also reported that this algorithm has the undesirable tendency to produce coincidental clusters (Barni *et al* 1996). Also, MEPFC depends heavily on initialization and often generates coincidental clusters since the objective function of this algorithm is separable. In addition, the 'scale parameter', β, depends on the data set and usually has to be determined experimentally (Bettinardi *et al* 1999). Even though the FCM is more sensitive to noise than PCM and MEPFC, it does not require parameters such as η and β to run. Furthermore, FCM is less sensitive to initialization than both PCM and MEPFC. For slightly noisy data, the performance of the FCM is not disturbed. However, for highly noisy data the performance of the FCM is affected. The aim of the present work is to tackle real data that could be reasonably noisy and not the challenging problem of highly noisy data.

The purpose of this work is to develop a powerful and robust segmentation tool, the use of which, in combination with morphological information provided by the cluster (sharp boundaries) to improve homogeneity within regions, allows us to reduce significantly the noise. Short transmission images in whole-body scanning can, therefore, be segmented into regions (clusters) of known attenuation coefficients (e.g. lungs, soft tissue and air). The final attenuation map is then calculated by combining the segmented and original images in a weighted fashion, using an approach similar to that described by Xu *et al* (1994, 1996), followed by adding up a previously acquired high statistics bed image.

2. Materials and methods

2.1. The fuzzy C-means segmentation algorithm

A basic problem that arises in a wide variety of fields, including pattern recognition, machine learning and statistics, is the so-called *clustering problem*. It plays a key role in searching for structures in data. Each of these structures is called *cluster*, a region in which the elements (objects) are as similar as possible. In this paper, data clustering is viewed as data partitioning problem. For partitioning data sets into groups of similar objects, it has been argued that fuzzy approaches often work better than crisp ones (Krishnapuram and Keller 1993, Beni and Liu 1994, Bezdek 1973, Trauwaert *et al* 1991, Roubens 1978). This is the case in many iterative algorithms, which converge to a local minimum of the objective function, without any assurance of its proximity to the global minimum. In this situation, a fuzzy clustering method evolves more smoothly to the global minimum whereas a crisp method bears more risk to get stuck in a local minimum (Rousseeuw *et al* 1995). In clustering-based image segmentation, the fuzzy approach is more reliable than the crisp one because grey

image possesses ambiguity within pixels due to the possible multi-valued levels of brightness in the image (Pal and Pal 1993). Incertitude in image pattern may be explained in terms of greyness ambiguity. For example, in medical image processing, the fuzzy approach is well suited because biological tissues have overlapping grey-scale intensity distributions due to imperfect image uniformity, noise and partial volume effects.

Consider a set of n vectors $X = \{x_1, x_2, \ldots, x_n\} \subset r^p$ to be clustered into $c \in \{1, 2, \ldots, n\}$ subsets that represent the structure of X. Each $x_k \in R^p$ is a feature vector consisting of p real-valued measurements (colour, length, ...) describing the features of the object represented by x_k. Clustering in unlabelled data X is the assignment of labels to objects generating X. c-partitions of X are sets of $(c \times n)$ values $\{\mu_{ik}\}$ that can be conveniently arranged as a $(c \times n)$ matrix $U = [\mu_{ik}]$. Each element, μ_{ik}, represents that the membership degree of x_k belongs to the ith cluster. The set of all $c \times n$ non-degenerate constrained fuzzy partitions, A_{cn}, is defined as follows:

$$A_{cn} = \left\{ U \in R^{c\times n} \;\middle|\; \sum_{i=1}^{c} \mu_{ik} = 1, \sum_{k=1}^{n} \mu_{ik} > 1 \quad \text{and} \right.$$
$$\left. \mu_{ik} \in [0, 1], i = 1, \ldots, c, 1 \leqslant k \leqslant n \right\} \subset [0, 1]^{c\times n}.$$

A well-known model of fuzzy clustering in X is the following objective function (Bezdek 1973):

$$J_m(U, V\colon X) = \sum_{k=1}^{n} \sum_{i=1}^{c} (\mu_{ik})^m \, \|x_k - v_i\|_A^2 .$$

$U \in A_{cn}$ is a fuzzy partition matrix, $m \in [1, +\infty[$ is a weighting exponent called the fuzzifier, $V = (v_1, v_2, \ldots, v_c)$ is a vector of unknown cluster centres (prototypes), $v_I \in R^p$ for $1 \leqslant i \leqslant c$ and $\|x\|_A = \sqrt{x^T A x}$ is any inner product norm where A is any positive definite matrix. Good partition U^* of X are taken from (U^*, V^*) that are local minimizers of J_m. The usual method to optimize J_m is to use partial optimization of U and V. That is, we first fix U and find necessary conditions on V to minimize J_m. Then, we fix V and minimize J_m with respect to U (Bezdek 1973). Approximate optimization of J_m by the FCM is based on the iteration:

$$\mu_{ik} = \left[\sum_{j=1}^{c} \left(\frac{\|x_k - v_i\|_A}{\|x_k - v_j\|_A} \right)^{\frac{2}{m-1}} \right]^{-1} \tag{1}$$

$$v_i = \frac{\sum_{k=1}^{n} \mu_{ik}^m x_k}{\sum_{k=1}^{n} \mu_{ik}^m}. \tag{2}$$

The FCM algorithm consists of iterations alternating between equations (1) and (2). This algorithm converges to either a local minimum or a saddle point of J_m (Bezdek 1973). In this work, feature vector x_k is restricted to the image grey-level value l. Thus, in the histogram-based FCM algorithm (Boudraa *et al* 2000), equations (1) and (2) are formulated as follows:

$$\mu_{il} = \left[\sum_{j=1}^{c} \left(\frac{\|l - v_i\|_A}{\|l - v_j\|_A} \right)^{\frac{2}{m-1}} \right]^{-1} \tag{3}$$

$$v_i = \frac{\sum_{l=0}^{L-1} \mu_{il}^m H(l) l}{\sum_{l=0}^{L-1} \mu_{il}^m} \tag{4}$$

where H represents the histogram of image of L-levels, where L is the number of grey levels. Each voxel has a feature that lies in the new discrete set $X = \{0, 1, \ldots, L-1\}$. The computation of membership degrees of $H(l)$ voxels is reduced to that of only one voxel with l as the grey-level value. The histogram-based FCM algorithm is outlined in the following steps:

(1) fix the number of clusters c, $2 \leqslant c \leqslant L$, and the threshold value ε;
(2) find the number of occurrences $H(l)$ of l, $l = 0, 1, \ldots, L-1$;
(3) initialize μ_{il} using the L grey levels such that

$$\sum_{i=1}^{c} \mu_{il} = 1 \qquad l = 0, 1, \ldots, L-1$$

(4) compute the centroid according to equation (4);
(5) update the membership degree $\tilde{\mu}_{il}$ according to equation (3);
(6) compute the defect measure

$$E = \sum_{i=1}^{c} \sum_{l=0}^{L-1} |\tilde{\mu}_{il} - \mu_{il}|$$

(7) if $(E > \varepsilon)$ $\{\mu_{il} \leftarrow \tilde{\mu}_{il}$ go to step 4$\}$;
(8) defuzzification process.

We use as many iterations as required until E is smaller than ε (in our case the threshold was fixed to 0.001). For the defuzzification process, every voxel is assigned to the cluster centre for which it has the maximum membership degree.

2.2. Attenuation correction and image reconstruction

The whole-body 3D tomograph installed at Geneva University Hospital, the ECAT ART (CTI/Siemens) was recently upgraded to use collimated point sources of ^{137}Cs and is capable of producing high-quality scatter-free data in this continuously rotating partial-ring tomograph (Watson *et al* 1997). This allows to increase the count statistics while drastically diminishing the acquisition time. There is a dual multi-slit collimator singles transmission source comprising two sets of 12 slits having an aperture ratio of 15:1 and axial pitch twice the axial crystal ring pitch. The images were scatter-corrected and reconstructed using normalized attenuation-weighted, ordered subset–expectation maximization iterative reconstruction (NAW OSEM) (Michel *et al* 1998). The default parameters used in clinical routine were applied (two iterations, eight subsets) followed by a post-processing Gaussian filter (kernel FWHM = 6.0 mm). The voxel size was set to $3.4 \times 3.4 \times 3.4$ mm^3.

When applying fuzzy clustering algorithms, a common task is to start with an oversized number of clusters. This is done to prevent the algorithm from misidentifying conflicting regions. Some of the problematic regions are the outer boundaries of the lungs and the brain skull. A merging process usually follows this overestimation in order to get the desired or natural number of clusters according to *a priori* anatomic knowledge.

PET transmission images were segmented using the FCM algorithm described above. The algorithm has been largely tested on different data sets, acquired under various timing protocols. Our experiments were valuable for optimizing the initial number of clusters (e.g. five in the thorax region). This overestimation of the actual regions present in the image greatly simplifies the merging process from five to three clusters. A contour detection algorithm is used to identify the external boundary of the thorax. From this initial segmentation, the bed is easily identified and can be removed using a mask filter. The filter gives back a binary image,

Figure 1. Illustration of the segmentation process of the heart/chest phantom transmission images showing from left to right: the original transmission image, FCM segmented image using five clusters, merging process to a three-clustered image (the bed is removed here), low-noise segmented image of the bed acquired and processed off-line, and the final attenuation map after applying a Gaussian filter and weighted averaging (the bed is added here).

where the soft tissue has one label and the background and lungs share another. In the final step, the lungs are identified using a labelling technique as outlined in Boudraa *et al* (1996, 2000), taking advantage of the fact that voxels belonging to the lungs are totally surrounded by soft tissue. A fast and efficient algorithm for image volume scanning and edge filling that avoids testing the condition on each voxel is used. Bone and soft tissue are considered as a single class since they are indistinguishable on typical short transmission scans.

The whole process is illustrated in figure 1. Once the transmission image is segmented, the tissue type corresponding to each label is identified (e.g. lungs, soft tissue, air). The attenuation map is then calculated by weighted averaging combining the segmented and original images using an approach similar to that described in Xu *et al* (1994, 1996). To this end, the voxels corresponding to lungs and soft tissue in the original reconstructed transmission images are scaled so that the averages within these regions are μ_{la} and μ_{sa}, respectively. The voxels within these regions are then filtered to reduce statistical noise and scaled to the expected attenuation density value. The hybrid attenuation map $f_h(x, y)$ is then calculated as follows:

$$f_h(x,y) = \begin{cases} w_s \mu_{s\mathrm{FCM}} + \frac{\mu_{st}}{\mu_{sa}} f_s(x,y) \times (1 - w_s) & \text{if} \quad (x,y) \in \text{soft tissue region} \\ w_l \mu_{l\mathrm{FCM}} + \frac{\mu_{lt}}{\mu_{la}} f_l(x,y) \times (1 - w_l) & \text{if} \quad (x,y) \in \text{lung region} \\ \mu_a = 0 & \text{if} \quad (x,y) \in \text{air region} \end{cases} \tag{5}$$

where μ_{st}, μ_{lt}, μ_{sa}, μ_{la} are the theoretical and average attenuation coefficients (obtained from the transmission image) for soft and lung tissues, respectively. $\mu_{s\mathrm{FCM}}$ and $\mu_{l\mathrm{FCM}}$ are the attenuation coefficients corresponding to the cluster centres of the segmented transmission image. The attenuation coefficient for air, μ_a, was neglected. The class-dependent weighting factors w_s and w_l control the degree to which the true values are emphasized (Anderson *et al* 1999), and were identical to the values reported in Xu *et al* (1996).

Subsequently, a high statistics transmission bed scan was acquired and the images were processed using the same reconstruction and processing protocol. This low-noise image of the bed is added up to the final segmented transmission images. The code was implemented to account for the different bed elevations between the bed scan and the clinical data sets by reading the appropriate information from the header of both images. The boundaries are then made more natural by applying a 5×5 Gaussian filter.

The proposed fuzzy clustering-based segmented attenuation correction (FCSAC) scheme was compared to both the standard measured attenuation correction (MAC) (Watson *et al* 1999) applied in clinical routine in our division and histogram thresholding-based segmented attenuation correction (TSAC) based on the work of Xu *et al* (1994, 1996) implemented within the ECAT 7.2 software supplied by the scanner manufacturer. In brief, the processing of the data sets entailed the following steps: the emission sinogram, normalization and reference scans together with the original transmission volume and AC matrix obtained using MAC were obtained for all data sets. The transmission images were thus segmented using both the FCM and thresholding techniques. The AC matrix is then calculated by forward projection

at appropriate angles of the resulting processed transmission image. The generated ACFs map was then used to correct the emission data. Qualitative and quantitative assessments of differences between images processed using the different protocols were performed by visual assessment and estimating the parameters of clinical interest (Zaidi *et al* 2001).

2.3. Phantom studies

Experimental phantom studies were performed to assess the accuracy and relative performance of the different protocols and their potential in clinical routine applications. Both the Alderson and chest/heart anthropomorphic phantoms were scanned and processed using the three protocols described above.

2.3.1. The Alderson phantom. The anthropomorphic Rando–Alderson phantom (Radiology Support Devices, Inc., Long Beach, CA) was used to assess the performance of the FCM segmentation algorithm. The phantom is made of tissue-equivalent materials that match human tissues in terms of mass density and attenuation characteristics. Transmission scans of 2, 3, 5 and 10 min corresponding to count statistics of 58, 151, 251 and 503 Mcounts, respectively, were acquired at the chest region. Transmission images were then segmented and compared with the original reconstructed images after full processing. We also assessed quantitative differences between the images in terms of average μ values and residual noise. The signal-to-noise ratio (SNR) defined as the average attenuation coefficient divided by the standard deviation of pixel intensities was calculated in large regions of interest (ROI) delineated within the lungs and soft-tissue regions.

2.3.2. The heart/chest phantom. The chest phantom simulates the lungs, heart cavity and spine contained within an elliptically shaped phantom (long and short axes of 30 and 20 cm). It consists of a top middle region containing heart cavity. Bottom left and right regions simulate the lungs (filled with sawdust). In the bottom centre, there is a cylinder of derlin, simulating the spine (figure 2(A)). The three heart cavity compartments were filled with a Ge-68 dissolution with activity concentrations ratios corresponding to 6.1:3:1 between wall:ventricular cavity:background, respectively, chosen to mimic average activity concentrations generally encountered in clinical [^{18}F]-fluorodeoxyglucose (FDG) studies. The transmission acquisition time was 10 min per bed position and a total of 50 Mcounts were collected for emission data in 3D mode. A typical transaxial slice of the transmission image is shown in figure 1 and a typical slice of PET myocardial wall images illustrated in figure 2(B). The activity of each compartment was carefully calibrated using a well counter. A total of 76 ROI were drawn in the different compartments of the heart phantom and background for images reconstructed using different protocols (MAC, TSAC and FCSAC), and the mean activity concentration (C_{avg}) within each ROI determined. The correlation between the results estimated using the different methods was then checked.

2.4. Clinical studies

The AC schemes were also tested on 22 patients with lung cancer referred to the Division of Nuclear Medicine of Geneva University Hospital for clinical evaluation of AC methods. All patients had plasma glucose checked before intravenous injection of 222 MBq of [^{18}F]-FDG adjusted to 70 kg body weight (none of them were diabetic), and PET images were obtained 90 min later. The acquisition time was 16 min per bed position (40% TX and 60% EM). For a quantitative analysis, we investigated the bias introduced and any significant differences in

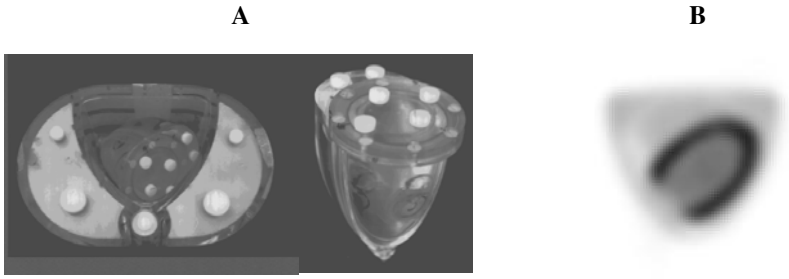

Figure 2. (A) Photograph of the heart/chest phantom and (B) typical reconstructed transaxial slice at the level of the myocardial wall.

the calculation of the standard uptake values (SUV) when using different protocols during the processing of the transmission scans. The SUV is a semi-quantitative index of [^{18}F]-FDG uptake commonly used to differentiate malignant from benign tumours and assess the efficacy of the therapy (Visvikis *et al* 2001).

With the advice of an experienced physician, manual ROI were drawn on the clinical studies that were diagnosed with lung cancer. We then calculated the maximum and average SUV values (SUV_{max} and SUV_{avg}), standard deviation (σ) and coefficient of variation (σ/SUV_{avg}), when transmission images were segmented using both the FCM and thresholding algorithms with respect to the values obtained using the standard measured transmission protocol. Sets of linear regression plots were then drawn between different processing techniques (Press 1992).

Quantitative evaluation of the difference between mean activity concentrations in phantom studies and SUV estimates in patient studies was performed using statistical analysis. A two-sample problem in the case of matched and correlated samples was used (Statsoft 2001). The student's *t*-test values and the corresponding significance levels associated with the student's analysis (one-tailed test) were calculated for the tumours' SUV estimates with FCSAC and TSAC as compared to the MAC technique (significant P value <0.01). It is worth pointing out that failure to prove statistically significant differences is not sufficient to confirm that the results are statistically identical.

3. Results

A detailed investigation was carried out to determine qualitative improvements and investigate quantitatively the correlation and statistically significant differences between the parameters of clinical interest when segmenting transmission images using the FCM algorithm, with respect to both MAC and TSAC methods.

3.1. Phantom studies

3.1.1. The Alderson phantom. Figure 3 illustrates the performance of the segmentation algorithm on the Alderson anthropomorphic phantom acquired with different timings. It can be clearly seen that the segmentation algorithm performs well even with short acquisition times on this low-sensitivity scanner (approximately 1/3 of the equivalent full-ring scanner, the ECAT EXACT). The contours of the lungs are well defined and the outer boundaries clearly and accurately delineated.

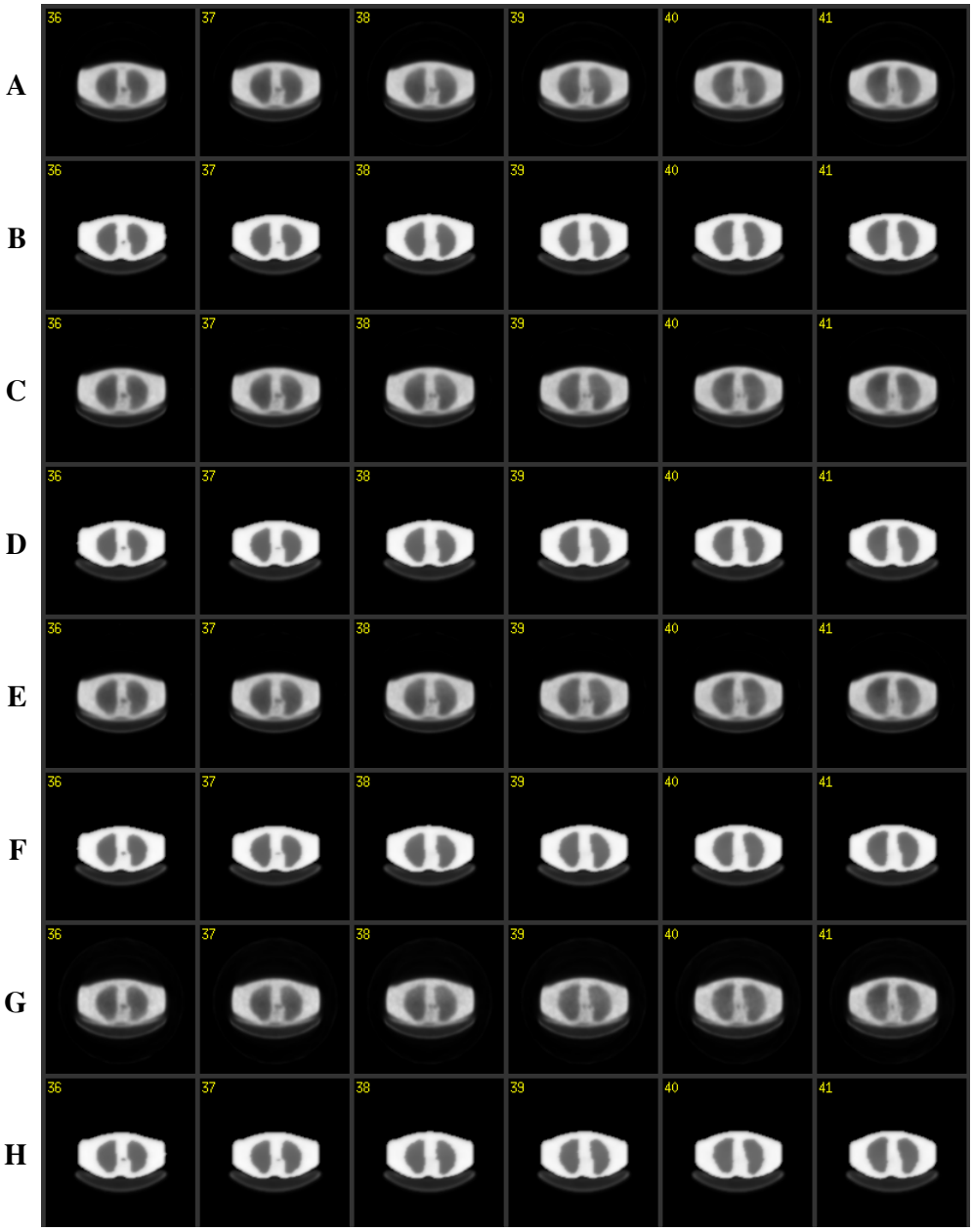

Figure 3. Illustration of the performance of the segmentation algorithm on the Alderson anthropomorphic phantom acquired with different timings. Unprocessed transmission images acquired in 10 min and FCM segmented attenuation map are shown in A and B, respectively. In cases C and D, E and F, and finally G and H, same as above for 5 min, 3 min and 2 min, respectively.

The quantitative analysis of the data revealed slight differences between the average attenuation coefficients in both the lung and soft-tissue regions when using different acquisition times and AC methods. Nevertheless, the segmented attenuation corrected images have higher SNR than the original MAC images (figure 4), which is more pronounced in the lung region.

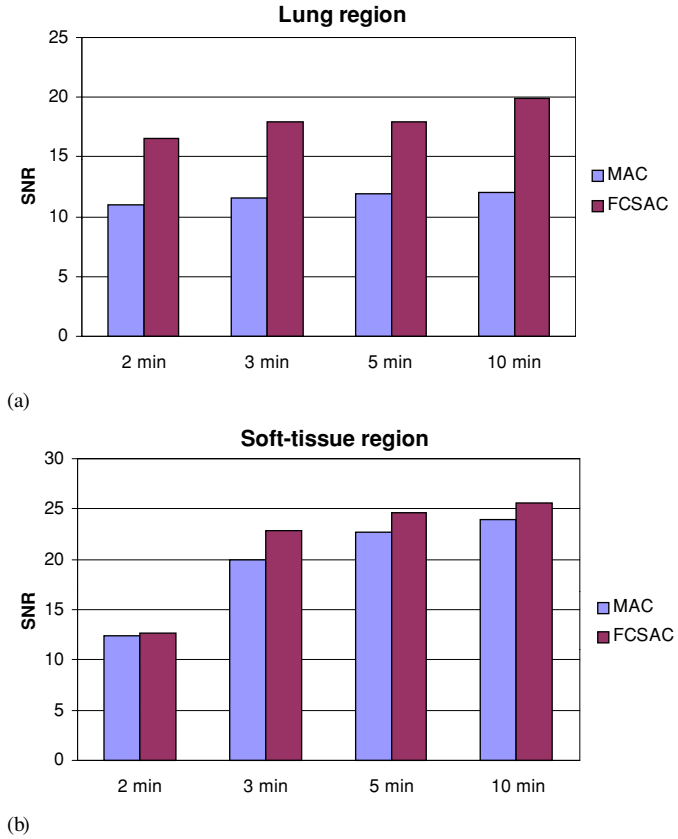

Figure 4. Plot of the SNR in both: (a) the lung and (b) the soft-tissue regions of the Alderson phantom.

The drastic improvement in SNR in the soft-tissue region when increasing the acquisition time in MAC is worth noting.

3.1.2. The heart/chest phantom. Figure 5 shows a series of linear regression plots illustrating the correlation between the different AC algorithms. The line connecting the data points represents the results of a linear regression analysis. There is a very good correlation ($R^2 = 0.96$) between MAC and FCSAC techniques and the regression line agreed well with the line of identity (slope = 1.01). The dispersion of data points is insignificant and the general trend as shown by the regression line is that the coefficients of variations are similar. However, TSAC leads to 3.5% lower overall estimates than MAC, whereas FCSAC leads to 1% higher estimates. An excellent correlation was also obtained between TSAC and FCSAC as well as between MAC and TSAC. The statistical comparison between absolute activity concentrations estimated using the different AC techniques is summarized in table 1. The per cent differences between the correction techniques are minor but statistically significant ($P < 0.01$).

3.2. Clinical studies

A representative slice of a clinical study at the level of the thorax is shown in figure 6 illustrating the original reconstructed and segmented images after the labelling process and

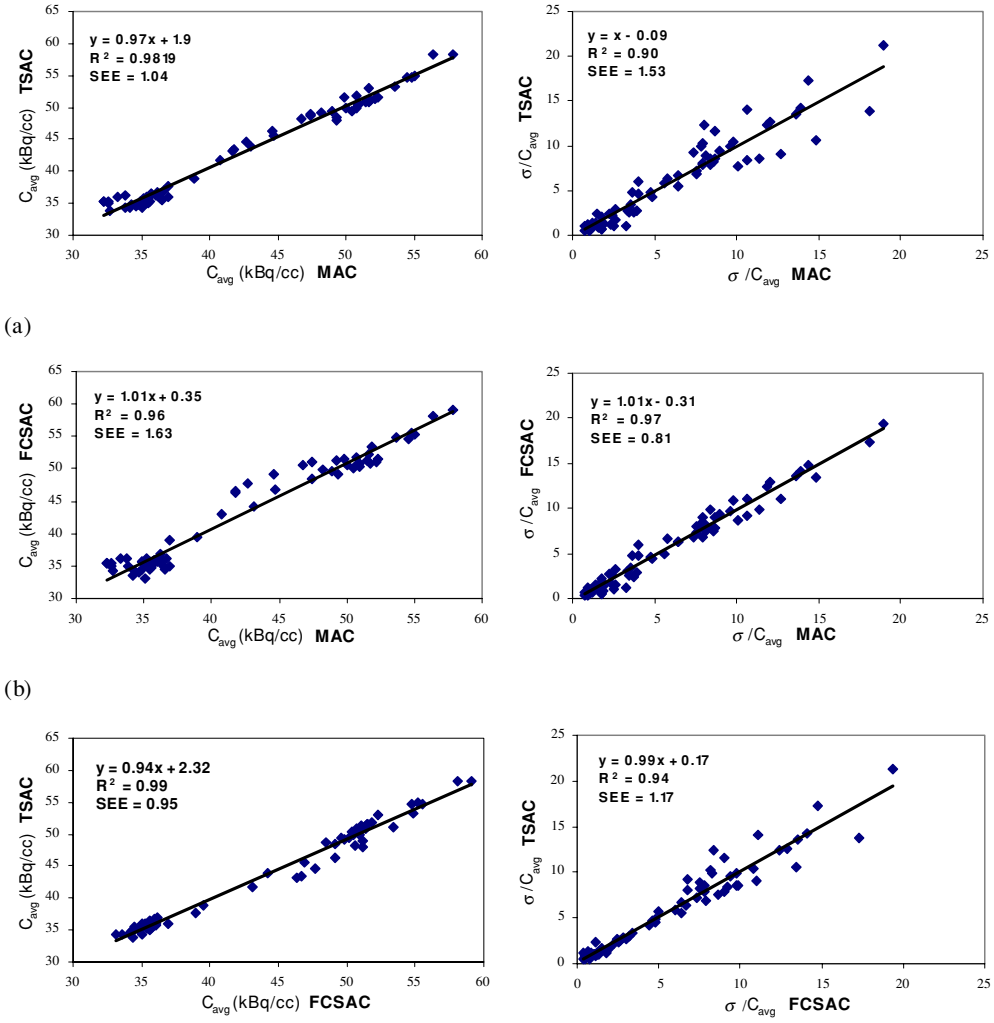

Figure 5. Correlation plots between heart phantom's average concentrations (C_{avg}) and coefficients of variations (σ/C_{avg}) when using different processing protocols: (a) MAC and TSAC, (b) MAC and FCSAC and (c) TSAC and FCSAC. Correlation coefficients, best fit equations and standard error of estimates are also included.

Table 1. Summary of statistical comparison between average activity concentrations in phantoms estimated using the usual MAC, TSAC and FCSAC protocols. The average per cent differences and associated statistical difference are shown. The critical t-value ($t_{\text{crit}} = 2.326$) is related to a probability of 0.01 for the null hypothesis to occur ('the two distributions are not the same').

Attenuation correction methods	% difference	Probability
MAC/TSAC	2.2 ± 2.2	<0.01
MAC/FCSAC	3.2 ± 3.2	<0.01
TSAC/FCSAC	1.8 ± 1.7	<0.01

Figure 6. Illustration of the fuzzy clustering segmentation algorithm on a clinical whole-body study at the thorax level showing from left to right: the reconstructed transmission image, the corresponding segmented image and the final attenuation map.

finally after assigning the tissue-dependent attenuation coefficients using weighted averaging. The improvement in image quality of emission data reconstructions when using FCSAC compared to MAC is further illustrated on coronal slices of a patient study in figure 7. The images are less noisy and show more uniform uptake of the tracer. In our clinic, MAC is applied routinely but the physicians preferred the images obtained with FCM-based segmented AC and judged the image quality to be much superior.

Figures 8–10 show the correlation between SUV estimates when using the different AC techniques. The line connecting the data points represents the results of a linear regression analysis. The results of the statistical analysis of the patient SUV data are summarized in table 2. These results further confirm the existence of a statistically significant difference between the different techniques, except MAC and FCSAC where no proof of statistically significant differences on the average SUVs was observed ($P = 0.27$, paired t-test). The reasons for this are not yet fully understood. Notwithstanding, the bias introduced when calculating tracer uptake in smaller lesions is less notable for the SUV_{avg} than the SUV_{max} due to partial volume effects, the latter being, however, more susceptible to increased levels of noise (Visvikis *et al* 2001). There was a good correlation ($R^2 = 0.96$) between maximum SUVs in lung nodules measured on images reconstructed with measured and segmented AC with a statistically significant decrease in SUV_{max} ($12.83 \pm 12.6\%$, $P < 0.01$) on the latter images. This would appear to result from a difference in the estimated and assigned μ values in the two cases and thus the ACFs applied. According to these data, the noise in MAC appears to be 19% higher overall than both TSAC and FCSAC. It is worth pointing out that the same observations were made by Watson *et al* (1999) when comparing pre- and post-injection transmission scanning. In the latter case, the differences in SUV estimates were assigned to patient motion and misregistration errors.

4. Discussion

The quantitative capability of PET measurements depends strongly on the accuracy of attenuation and scatter corrections. While scatter correction in whole-body PET imaging is only approximate and has limited accuracy (Zaidi 2001), AC is exact and is limited mainly by the statistics of the acquired data. Reliable AC methods for quantitative ECT require precise delineation of the body contour and accurate knowledge of the distribution of attenuation coefficients. Two broad classes of methods have been used to calculate the attenuation map referred to as calculated- and measured-based AC techniques. In clinical applications, where the attenuation coefficient distribution is not known *a priori*, and for areas of inhomogeneous attenuation such as the chest, more adequate methods must be performed.

Figure 7. Illustration of the improvement in image quality when using segmented AC: (A) reconstructions using MAC, (B) reconstructions using FCSAC.

This includes transmission scanning (Bailey 1998), segmented MRI data (Rowell *et al* 1992) or appropriately scaled x-ray CT scans acquired either independently on separate (Kinahan *et al* 1998) or simultaneously on multi-modality imaging systems (Beyer *et al* 2000). The CT scans produce images of high spatial resolution and statistical accuracy. These images are, however, produced by bremsstrahlung photons with a broad energy distribution, which may affect the accuracy of the determination of the attenuation coefficients. Moreover, the cost of combined ECT/CT systems remains prohibitive for small nuclear medicine departments and combination of data acquired from different imagers suffer from the usual problems of working with multi-modality images, namely, accurate coregistration from different modalities. Alternative methods to compensate for photon attenuation use either continuous (Welch *et al* 1998) or discrete consistency conditions criteria (Bronnikov 2000).

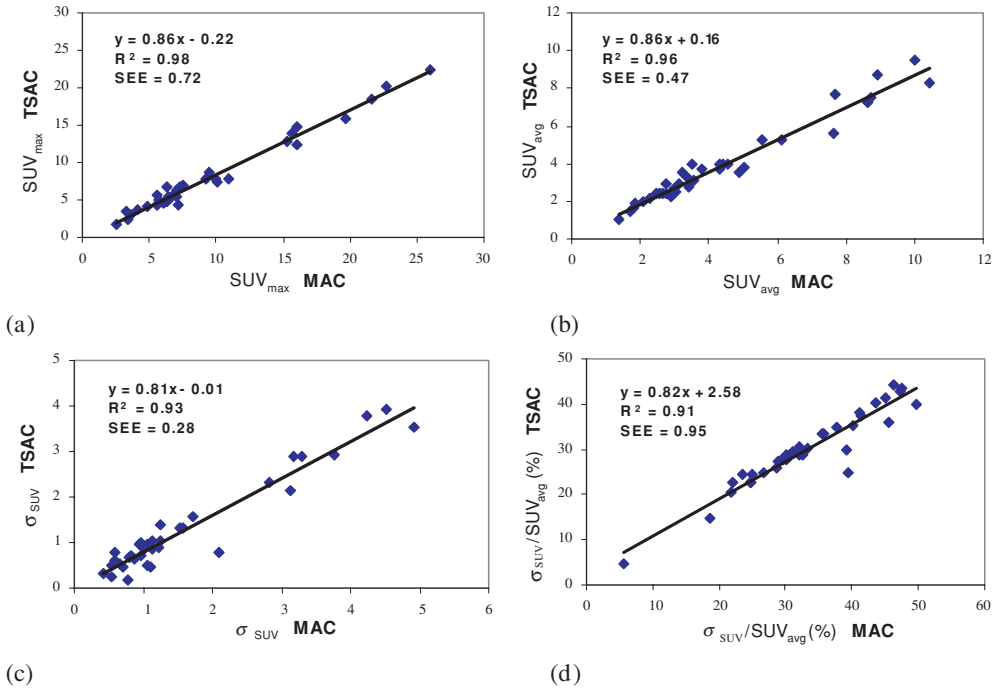

Figure 8. Correlation plots between patients' SUV estimates obtained using MAC and TSAC: (a) maximum SUV (SUV_{max}), (b) average SUV (SUV_{avg}), (c) the standard deviation (σ) and finally (d) the coefficient of variation (σ/SUV_{avg}). Correlation coefficients, best fit equations and standard error of estimates are also included.

In a clinical environment, the most accurate AC techniques are based on measured transmission data acquired before (pre-injection) (Watson *et al* 1999), during (simultaneous) (Watson *et al* 2001) or after (post-injection) (Smith *et al* 1997) the emission scan. More refined transmission image segmentation and tissue classification tools were also proposed to increase the accuracy of AC when using short transmission scanning times (Meikle *et al* 1993, Xu *et al* 1996). Once the attenuation map is obtained, the correction matrix is calculated by forward projection at appropriate angles of the resulting processed transmission image. From a clinical perspective, the relative benefits of segmented AC seem to be well recognized in clinical oncology (Benard *et al* 1999). From a theoretical analysis, the fuzzy clustering approach is more versatile than histogram-based methods in segmenting complex anatomic areas, allowing good preservation of density gradients in the lungs.

A number of factors influence the accuracy of AC in PET imaging when one uses histogram-based threshold edge detection methods. One common difficulty with this approach is determining the value of the thresholds. As stated by many authors, no single threshold is ideal for all object shapes and sizes (Zaidi 1996) and each group picked the threshold that best matched their specific phantom or clinical studies, transmission source type and imaging system (Bilger *et al* 2001). Clustering methods need to be robust and reproducible if they are to be useful in practice. Fuzzy clustering is a robust, model-independent method to extract anatomical and functional information. It improves the reproducibility of transmission image segmentation significantly because of the capability of fuzzy clustering to separate the regions with different properties by solving the problem of volume averaging of tissue compartments.

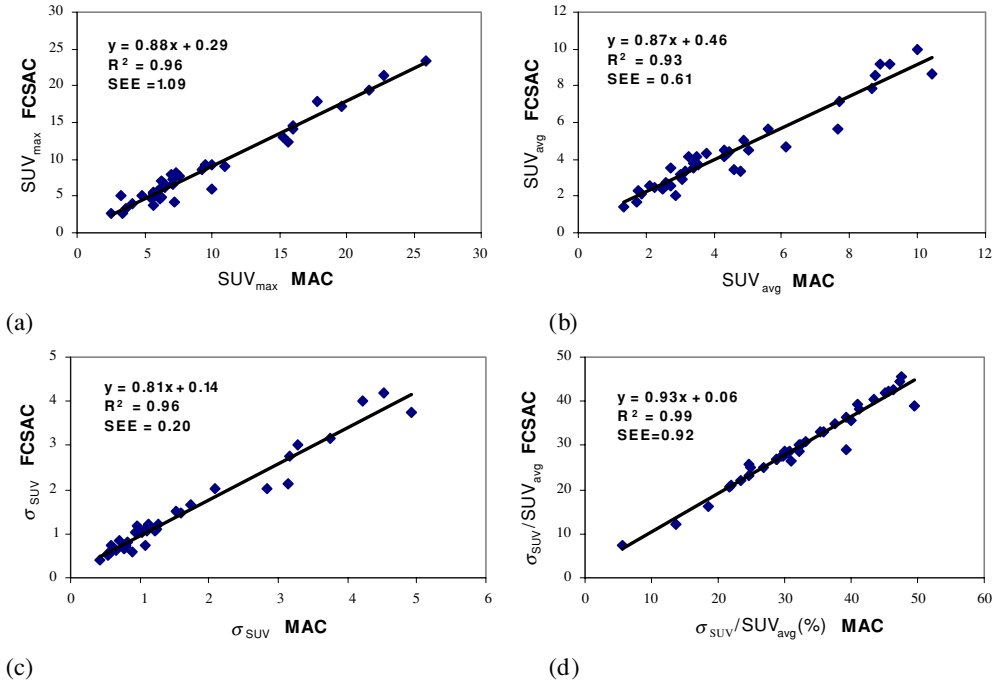

Figure 9. Correlation plots between patients' SUV estimates obtained using MAC and FCSAC: (a) maximum SUV (SUV_{max}), (b) average SUV (SUV_{avg}), (c) the standard deviation (σ) and finally (d) the coefficient of variation (σ/SUV_{avg}). Correlation coefficients, best fit equations and standard error of estimates are also included.

Other interesting approaches to segment noisy transmission data include the use of active contour models (Tai *et al* 1996), neural networks (Yu and Nahmias 1996), morphological segmentation (Riddell *et al* 1999) and hidden Markov modelling (Anderson *et al* 1999). An alternative to segmentation of transmission images with the aim to reduce noise in PET transmission measurements includes Bayesian image reconstruction (Alenius *et al* 1999) and non-linear filtering (Kitamura *et al* 2000).

In summary, we developed a fuzzy clustering-based segmentation technique for AC in PET, which allows the segmentation of transmission images into the main anatomical regions of the body in terms of the corresponding attenuation coefficient values. The algorithm was implemented in the C++ language and runs on a SUN Sparc station 60. It is fast, efficient, accurate and relatively operator-independent to allow application in clinical routine. Furthermore, it does not depend on statistical assumptions such as data normality, nor does it require any *a priori* heuristics. One limitation of the algorithm concerns patients whose lung contours extend up to the thorax boundary at the interface with the bed. This was encountered only in one patient and required operator interaction to make the method work. We recently started to use the dual/fusion display software (Lartizien *et al* 2000), which proved to be useful for dual display and comparison of the segmented and original transmission images. This might be very helpful to identify possible pitfalls of the algorithm, which could produce artefacts in the reconstructed emission images. This segmentation technique is actually being optimized for automated lesion detection and quantification of lung nodules' size and uptake in cancer patients using PET imaging to improve reproducibility of the analysis and reduce an expert physician's interaction.

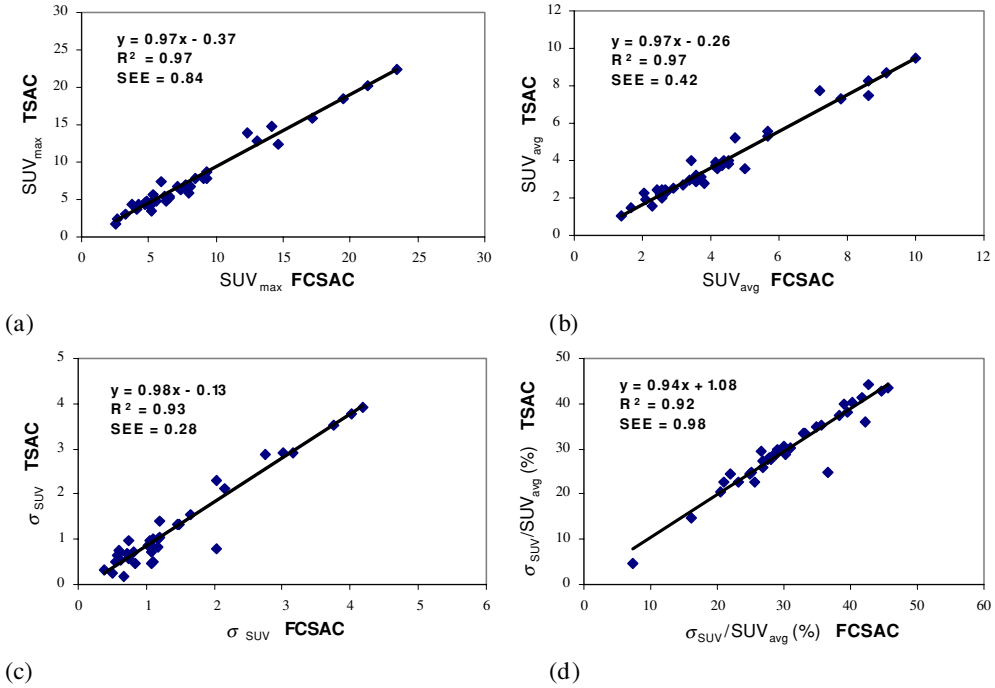

Figure 10. Correlation plots between patients' SUV estimates obtained using TSAC and FCSAC: (a) maximum SUV (SUV_{max}), (b) average SUV (SUV_{avg}), (c) the standard deviation (σ) and finally (d) the coefficient of variation (σ/SUV_{avg}). Correlation coefficients, best fit equations and standard error of estimates are also included.

Table 2. Summary of statistical comparison between clinical average and maximum SUV data estimated using the usual MAC, TSAC and FCSAC protocols. The average per cent differences and associated statistical difference are shown. The critical t-value ($t_{crit} = 2.326$) is related to a probability of 0.01 for the null hypothesis to occur ('the two distributions are not the same').

Attenuation correction methods	SUV_{avg}		SUV_{max}	
	% difference	Probability	% difference	Probability
MAC/TSAC	12.02 ± 7.9	<0.01	17.03 ± 8.4	<0.01
MAC/FCSAC	11.06 ± 10.1	$\gg 0.20$	12.83 ± 12.6	<0.01
TSAC/FCSAC	12.30 ± 7.5	<0.01	11.8 ± 8.0	<0.01

5. Conclusions

The addition of fuzzy clustering-based segmentation to the attenuation correction process in [^{18}F]-FDG PET markedly improves image quality and lesion-to-background contrast compared to the standard measured attenuation correction technique. This resulted in an improved lesion detection rate in patients with lung cancer, diagnostic performance and more accurate staging. Moreover, FCM-based segmented attenuation correction in PET shows a clear reduction of noise propagation from transmission into emission data with respect to MAC, allowing for reduction of transmission scan duration. In spite of the promising results obtained so far, its additional impact on patient management in this relatively small sample was minor; further study of this most important outcome in a larger study is warranted. It is acknowledged,

however, that no conclusions could be drawn from this study regarding the performance of the FCM method relative to other fuzzy clustering-based methods (e.g. Bettinardi *et al* 1999).

Acknowledgments

This work was supported by the Swiss National Science Foundation under grant number SNSF 3152–062008. The authors would like to thank Dr Mohamed Allaoua for his help during the analysis of the clinical data and Dr Paul Kinahan for supplying the dual/fusion display software.

References

Acton P D, Lyn S, Pilowsky Kung H F and Peter J E 1999 Automatic segmentation of dynamic neuroreceptor single-photon emission tomography images using fuzzy clustering *Eur. J. Nucl. Med.* **26** 581–90

Alenius S, Ruotsalainen U and Astola J 1999 Attenuation correction for PET using count-limited transmission images reconstructed with median root prior *IEEE Trans. Nucl. Sci.* **46** 646–51

Anderson J M M, Mair B A and Rao M 1999 Attenuation correction for PET using a hidden Markov model based segmentation method *Proc. IEEE Nuclear Science Symp. and Medical Imaging Conf. (1999)*

Bailey D L 1998 Transmission scanning in emission tomography *Eur. J. Nucl. Med.* **25** 774–87

Barni M, Cappellini V and Mecocci A 1996 Comments on a possibilistic approach to clustering *IEEE Trans. Fuzzy System* **4** 393–6

Benard F, Smith R J, Hustinx R, Karp J S and Alavi A 1999 Clinical evaluation of processing techniques for attenuation correction with 137Cs in whole-body PET imaging *J. Nucl. Med.* **40** 1257–63

Beni G and Liu X 1994 A least biased fuzzy clustering method *IEEE Trans. Pattern Anal. Machine Intell.* **16** 954–60

Bettinardi V *et al* 1999 An automatic classification technique for attenuation correction in positron emission tomography. *Eur. J. Nucl. Med.* **26** 447–58

Beyer T, Townsend D W, Brun T, Kinahan P E, Charron M, Roddy R, Jerin J, Young J, Byars L and Nutt R 2000 A combined PET/CT scanner for clinical oncology *J. Nucl. Med.* **41** 1369–79

Bezdek J C 1973 *Fuzzy Mathematics in Pattern Classification* (New York: The Institute of Electrical and Electronics Engineers)

Bezdek J C, Hathaway R J, Sabin M J and Tucker W T 1987 Convergence theory for fuzzy C-means: counterexamples and repairs *IEEE Trans. Syst. Man Cybern.* **17** 873–7

Bilger K, Kupferschlager J, Muller-Schauenburg W, Nusslin F and Bares R 2001 Threshold calculation for segmented attenuation correction in PET with histogram fitting *IEEE Trans. Nucl. Sci.* **48** 43–50

Boudraa A E, Champier J, Cinotti L, Bordet J C, Lavenne F and Mallet J J 1996 Delineation and quantitation of brain lesions by fuzzy clustering in positron emission tomography *Comput. Med. Imaging Graph* **20** 31–41

Boudraa A O, Dehak S M, Zhu Y M, Pachai C, Bao Y G and Grimaud J 2000 Automated segmentation of multiple sclerosis lesions in multispectral MR imaging using fuzzy clustering *Comput. Biol. Med.* **30** 23–40

Bronnikov A V 2000 Reconstruction of attenuation map using discrete consistency conditions *IEEE Trans. Med. Imaging* **19** 451–62

Dunn J C 1974 A fuzzy relative of the ISODATA process and its use in detecting compact well-separated clusters *J. Cybern.* **3** 32–57

Kinahan P E, Townsend D W, Beyer T and Sashin D 1998 Attenuation correction for a combined 3D PET/CT scanner *Med. Phys.* **25** 2046–53

Kitamura K, Iida H, Shidahara M, Miura S and Kanno I 2000 Noise reduction in PET attenuation correction using non-linear Gaussian filters *IEEE Trans. Nucl. Sci.* **47** 9949

Krishnapuram R and Keller J M 1993 A possibilistic approach to clustering *IEEE Trans. Fuzzy Syst.* **1** 98–110

Lartizien C, Kinahan P E, Comtat C, Lin M P, Swensson R, Trebossen R and Bendriem B 2000 Evaluating image reconstruction methods for tumor detection performance in whole-body PET oncology imaging *Proc. SPIE Medical Imaging Symp. (San Diego, CA, 2000)*

Lonneux M, Borbath I, Bol A, Coppens A, Sibomana M, Bausart R, Defrise M, Pauwels S and Michel C 1999 Attenuation correction in whole-body FDG oncological studies: the role of statistical reconstruction *Eur. J. Nucl. Med.* **26** 591–8

Meikle S R, Dahlbom M and Cherry S R 1993 Attenuation correction using count-limited transmission data in positron emission tomography *J. Nucl. Med.* **34** 143–150

Michel C, Sibomana M, Boi A, Bernard X, Lonneux M, Defrise M, Comtat C, Kinahan P E and Townsend D W Preserving Poisson characteristics of PET data with weighted OSEM reconstruction *Proc. IEEE Nuclear Science Symp. and Medical Imaging Conf. (1998)*

Pal N R and Bezdek J C 1995 On cluster validity for the fuzzy C-means model *IEEE Trans. Fuzzy Syst.* **3** 370–9

Pal N R and Pal S K 1993 A review on image segmentation techniques *Pattern Recognition* **25** 1277–94

Press W H 1992 *Numerical Recipes in C, the Art of Scientific Computing* (Cambridge: Cambridge University Press)

Reutte B, Klein G J and Huesman R H 1997 Automated 3-D segmentation of respiratory-gated PET transmission images *IEEE Trans. Nucl. Sci.* **44** 2473–6

Riddell C, Brigger P, Carson R E and Bacharach S L 1999 The watershed algorithm: a method to segment noisy PET transmission images *IEEE Trans. Nucl. Sci.* **46** 713–9

Roubens M 1978 Pattern recognition problem with fuzzy sets *Fuzzy Sets Syst.* **1** 239–53

Rousseeuw P J, Trauwaert E and Kaufman L 1995 Fuzzy clustering with high contrast *J. Comput. Appl. Math.* **64** 81–90

Rowell N P, Glaholm J, Flower M A, Cronin B and McCready V R 1992 Anatomically derived attenuation coefficients for use in quantitative single photon emission tomography studies of the thorax *Eur. J. Nucl. Med.* **19** 36–40

Smith R J, Karp J S, Muehllehner G, Gualtieri E and Benard F 1997 Singles transmission scans performed post-injection for quantitative whole body PET imaging *IEEE Trans. Nucl. Sci.* **44** 1329–35

Statsoft 2001 *Statsoft Electronic Statistics Textbook* (Tulsa, OK: Statsoft)

Tai Y-C, Lin K-P, Dahlbom M and Hoffman E J 1996 A hybrid attenuation correction technique to compensate for lung density in 3-D total body PET *IEEE Trans. Nucl. Sci.* **43** 323–30

Trauwaert E, Kaufman L and Rousseeuw P 1991 Fuzzy clustering algorithms based on maximum likelihood principle *Fuzzy Sets Syst.* **42** 213–27

Visvikis D, Cheze-LeRest D, Costa D C, Bomanji J, Gacinovic S and Ell P 2001 Influence of OSEM and segmented attenuation correction in the calculation of standardised uptake value for [18F] FDG PET *Eur. J. Nucl. Med.* **28** 1326–35

Watson C C, Eriksson L, Casey M E, Jones W F, Moyers J C, Miller S, Hamill J, Van Lingen A, Bendriem B and Nutt R 2001 Design and performance of collimated coincidence point sources for simultaneous transmission measurements in 3-D PET *IEEE Trans. Nucl. Sci.* **48** 673–9

Watson C C, Jones W, Brun T, Baker K, Vaigneur K and Young J 1997 Design and performance of a single photon transmission measurement for the ECAT ART *Proc. IEEE Nuclear Science Symp. and Medical Imaging Conf. (1997)*

Watson C C, Schaefer A, Luk W K and Kirsch C M 1999 Clinical evaluation of single-photon attenuation correction for 3D whole-body PET *IEEE Trans. Nucl. Sci.* **46** 1024–31

Welch A *et al* 1998 Attenuation correction in PET using consistency information *IEEE Trans. Nucl. Sci.* **45** 3134–41

Xie X L and Beni G 1991 A validity measure for fuzzy clustering *IEEE Trans. Pattern Anal. Machine Intell.* **13** 841–7

Xu M, Cutler P and Luk W 1996 An adaptive local threshold segmented attenuation correction method for whole-body PET imaging *IEEE Trans. Nucl. Sci.* **43** 331–6

Xu M, Luk W K, Cutler P D and Digby W M 1994 Local threshold for segmented attenuation correction of PET imaging of the thorax *IEEE Trans. Nucl. Sci.* **41** 1532–7

Yu S K and Nahmias C 1996 Segmented attenuation correction using artificial neural networks in positron tomography *Phys. Med. Biol.* **41** 2189–206

Zaidi H 1996 Organ volume estimation using SPECT *IEEE Trans. Nucl. Sci.* **43** 2174–82

Zaidi H 2001 Scatter modelling and correction strategies in fully 3D PET *Nucl. Med. Commun.* **22** 1181–4

Zaidi H, Diaz-Gomez M, Boudraa A E and Slosman D O 2001 Attenuation correction for whole-body PET imaging using automated fuzzy clustering-based segmentation method *Proc. IEEE Nuclear Science Symp. and Medical Imaging Conf. (San Diego, CA, 2001)*